Phonon softening and electron-phonon coupling in the topological nodal-line semimetal ZrGeSe

Weiyao Zhao [1,2,*] Enamul Haque [2,*] Lei Guo,[3] David Cortie [4,5] Lei Chen,[6] Bahadir Salmankurt [7] Xiaolin Wang,[1]
Ren-Kui Zheng,[6] Nikhil V. Medhekar [2] Julie Karel,[2] and Kirrily C. Rule [4,5,†]

[1]*Institute for Superconducting and Electronic Materials and ARC Centre of Excellence in Future Low-Energy Electronics Technologies,
University of Wollongong, Wollongong, New South Wales 2500, Australia*
[2]*Department of Materials Science and Engineering and ARC Centre of Excellence in Future Low-Energy Electronics Technologies,
Monash University, Clayton, Victoria 3800, Australia*
[3]*School of Physics, Southeast University, Nanjing 211189, China*
[4]*School of Physics, University of Wollongong, Wollongong, New South Wales 2522, Australia*
[5]*Australian Nuclear Science and Technology Organisation, Lucas Heights, New South Wales 2234, Australia*
[6]*School of Physics and Materials Science, Guangzhou University, Guangzhou 510006, China*
[7]*Distance Education Center, Sakarya University of Applied Sciences, Sakarya 54001, Turkey*

ZrGeSe is one of the most well-known topological nodal-line semimetals, which possesses linearly dispersive electronic bands near the Fermi surface. However, the lattice-dynamics study and its interaction with the electronic system have not been investigated. We employed the inelastic neutron-scattering method to study the lattice dynamics of ZrGeSe single crystals. The measured acoustic phonon dispersions were compared with lattice-dynamics calculations, with an overall good agreement with theory; however, both the longitudinal and the transverse acoustic phonon dispersions along the (q00) directions demonstrate significant softening, unexpectedly in contrast with the theoretical predictions. Complementary *ab initio* molecular dynamics simulations indicate an anomalous temperature dependency in the vibrational spectroscopy. We show that strong electron-phonon coupling exists along the Γ-*M-X* directions and argue that the phonon softening is induced by such electron-phonon coupling.

I. INTRODUCTION

The concept of *topology* is now widely used in condensed matter physics, which describes the unique properties of certain materials' electronic band structure. Recently, advanced theoretical analyses based on point-group symmetry were employed to predict the topology in materials [1]. Topological materials offer unique advantages in their electronic transport properties such as ultrahigh mobility, ultralow dissipation, and built-in spin polarization. These potentially enable more energy-efficient electronic devices to be built, which may serve better than traditional silicon. The topology of electronic band structures of materials can be categorized according to the type of (conduction and valence) band crossing behavior they exhibit, i.e., a Dirac semimetal occurs when the bands cross at a fourfold degenerate point (Dirac point), and a Weyl semimetal is a system where the Dirac point splits into two sets of twofold degenerate points [2]. We can also classify a material in which the conduction bands cross the valence bands through a closed curve, as a topological nodal-line semimetal (TNLS) [3]. The band crossing points are the source of the quantum electronic transport properties, and it is therefore important to study the precise interactions, including electron-phonon interactions, that modify the details of the underlying band structure at the low-energy meV scale in TNLSs.

Among the TNLS materials, Zr*YZ*'s (*Y* = Si, Ge, and Sn; *Z* = S, Se, and Te) are among the most studied compounds [4–11]. The Zr*YZ* compounds crystallize in the PbFCl structure, which is described by the tetragonal *P4/nmm* space group. The electronic band topology of those compounds and transport behavior are well studied, and the past work has included both magnetotransport [11] and angular-resolved photoemission spectroscopy experiments [10]. Experimental data on the phonon band structures, however, remains scarce. The phonon band structure and thermal properties of these materials are also important, as these impact the finite-temperature transport including the crossover from the quantum to the semiclassical regime, which is highly relevant to potential electronic and thermoelectric applications. From density functional theory (DFT) calculations [12], the phonon modes of ZrSiS, ZrSiSe, ZrGeS, and ZrGeSe have highly dispersive acoustic phonons and low-lying optical phonons, producing a gapless total density of states (DOS). Although those compounds are structurally very similar, the phonon excitations are significantly different from one to another, e.g., the highest energy optical phonon mode (ω_{max}) is determined purely by the lightest element: Si in ZrSiS (~52 meV) and ZrSiSe (~47 meV) or S in ZrGeS (~42 meV), whereas ZrGeSe is a special case. Specifically, in ZrGeSe, given the comparable masses of Zr, Ge, and Se, all three elements theoretically contribute to the total phonon DOS

---

*These authors contributed equally to this work.
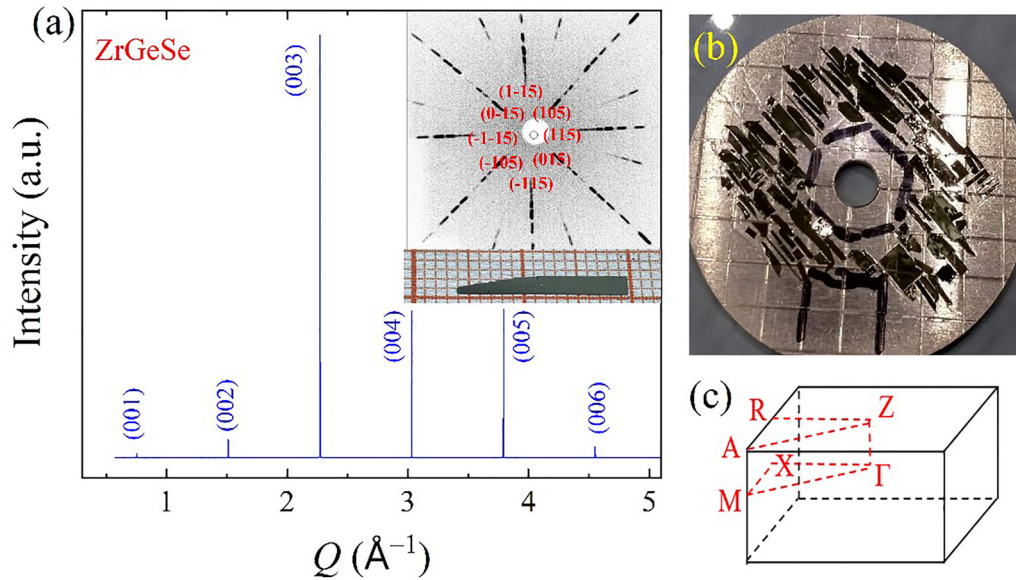†kirrily@ansto.gov.au

FIG. 1. (a) Single crystal x-ray diffraction patterns of ZrGeSe. Inset graph: x-ray Laue diffraction patterns, and photo of a ZrGeSe single crystal piece. (b) The mosaic structure of coaligned ZrGeSe crystals on an Al disk. (c) A sketch of the reciprocal space of ZrGeSe.

including the highest optical modes, which are predicted to lie around 31 meV [12]. In addition to this, recently, theoretical calculations showed that the Weyl-like and nodal-line-like phonon degenerate bands exist in real materials [13–16] and this in turn motivates further experimental examination of the phonons in the Zr*YZ* family. The topological phonon structures are always related to specific atomic lattice vibrations, and therefore lead to abnormal heat transport behavior, e.g., the phonon Hall effect [17] and phonon-glass and electron-crystal phenomenon [18]. The topological band structures are protected by the symmetries of the materials, therefore the electronic topological materials most likely also host topological phonon bands, e.g., the tripoint band degenerate behavior in other topological semimetals such TaSb and TaBi arise both in electronic and in phonon band structures [18]. Due to the difficulty in obtaining large bulk crystals, however, the experimental confirmation of the phonon spectra, including the determination of ω_{max}, in this compound is still lacking.

To experimentally probe the lattice dynamics of this family of TNLS materials, we have investigated the lattice dynamics in ZrGeSe single crystals via inelastic neutron scattering. After comparing the experimental observation with first-principles calculations at 0 K, we found that the observed acoustic phonons along the Γ-*M* directions are softer than the theoretical predictions. The *ab initio* molecular dynamics (AIMD) simulation at experimental temperatures, however, fits the observation better, which suggests strong temperature dependency of the phonon bands in ZrGeSe. We show that it is likely that strong electron-phonon coupling in these directions is the mechanism for the observed phonon softening.

II. EXPERIMENTS AND SIMULATIONS

A. Single crystal growth

Single crystals of ZrGeSe were grown via chemical vapor transport as described elsewhere [11]. The single crystals

grown from this method are typically thin, rectangular plates, as seen in the inset of Fig. 1(a), with the normal vector along the (001) direction, and both long and short edges along the (110) direction. The single crystal x-ray diffraction patterns are shown in Fig. 1(a), in which the sharp comblike (00*l*) peaks illustrate the good crystal quality and perfect orientation of the crystal sheets in the out-of-plane direction. To verify the in-plane orientation, x-ray Laue diffraction revealed the symmetry at room temperature, which is shown in the inset of Fig. 1(a). Sharp diffraction points were indexed via the *P*4/*nmm* space group, indicating that the edges of the crystals were defined as the (110) direction, or equivalent axes.

B. Neutron scattering

We employed the neutron thermal triple-axis spectrometer, Taipan, at the Australian Nuclear Science and Technology Organisation (ANSTO), to study the lattice dynamics in TNLS ZrGeSe single crystals. The observation of both acoustic and optical phonons was thus used to determine the validity and robust nature of the DOS models for ZrGeSe.

Due to the regular shape of the ultrathin, single crystals, around 100 pieces were coaligned on an aluminum disk using the low-hydrogen amorphous fluoropolymer glue, CYTOP [see Fig. 1(b)] [19]. This allowed us to prepare a quasi-single crystal sample with a mass of approximately 0.1 g, as required for inelastic neutron-scattering measurements. Due to the small sample mass, Taipan was configured with an open-open-open-open collimation and a double-focused monochromator and analyzer using the fixed $E_f = 14.87$ meV, affording an energy resolution of 1 meV. The data were collected in both the $\Gamma(2,0,0)$-X(3,0,0) and $\Gamma(0,0,3)$-Z(0,0,3.5)-*R*(1,0,3.5) planes by performing constant-*Q* energy scans. Note that the high-symmetry points are labeled using the conventional symbols for the *P*4/*nmm* space group, which is shown in Fig. 1(c). The coaligned samples were installed in a closed-cycle cryostat, and measured at 25 and 300 K.

C. Simulation methods

Phonon measurements were compared with recently published calculations that were performed using density functional theory with the details given in Ref. [12]. Additional calculations were performed using the Vienna *Ab initio* Simulation Package (VASP) along with PHONOPY [20]. The GGA-PBE exchange functional was used [21] together with Grimme's D2 van der Waals correction [22]. AIMD simulations were performed for $4 \times 4 \times 2$ and $3 \times 3 \times 4$ supercells of ZrGeSe containing more than 200 atoms. Calculations were performed in the Born-Oppenheimer approach, and a Nose-Hoover thermostat at either 300 or 25 K. Experimental lattice constants of $a = 3.706$ Å and $c = 8.271$ Å were used in AIMD calculations. The trajectories were visualized using the VISUAL MOLECULAR DYNAMICS software [23]. To enable comparison with the neutron spectroscopy measurements, the trajectories were postprocessed to calculate the neutron-scattering function from the Fourier transform of the intermediate scattering function as described below:

$$S(\mathbf{q}, \omega) = \frac{1}{2\pi} \int_{-\infty}^{+\infty} dt \, \exp[-i\omega t] F(\mathbf{q}, t). \tag{1}$$

$F(\mathbf{q}, t)$ is called the intermediate scattering function and is defined as

$$F(\mathbf{q}, t) = \sum_{\alpha, \beta} \Gamma_{\alpha\beta\langle \exp[-i\mathbf{q}\cdot\hat{\mathbf{R}}_\alpha(0)] \exp[i\mathbf{q}\cdot\hat{\mathbf{R}}_\beta(t)] \rangle}, \tag{2}$$

$$\Gamma_{\alpha\beta} = \frac{1}{N}\left[\overline{b_\alpha}\,\overline{b_\beta} + \delta_{\alpha\beta}\left(\overline{b_\alpha^2} - \overline{b_\alpha}^2\right)\right]. \tag{3}$$

The operators $\hat{\mathbf{R}}_\alpha(t)$ in Eq. (2) are the position operators of the nuclei in the sample, and $\mathbf{q}$ is the reciprocal lattice vector. The brackets $\langle \cdots \rangle$ denote a quantum thermal average and the time dependence of the position operators is defined by the Heisenberg picture. The quantities b_α are the coherent/incoherent scattering lengths of the nuclei, which depend on the isotope and the relative orientation of the spin of the neutron and the spin of the scattering nucleus. The overbars appearing in $\Gamma_{\alpha\beta}$ denote an average over (naturally abundant) isotopes and uncorrelated, random spin orientations of the neutron and nucleus, as appropriate for the experimental conditions in this work. Additionally, the density of states was calculated using the velocity autocorrelation function (VACF) obtained from the trajectories, as implemented in the NMOLDYN software [24]. Mathematically, the VACF of atom α in an atomic or molecular system is usually defined as

$$C_{vv;\alpha\alpha}(t) \doteq \frac{1}{3}\langle \mathbf{v}_\alpha(t_0) \cdot \mathbf{v}_\alpha(t_0 + t)\rangle_{t0}. \tag{4}$$

In some cases, e.g., for nonisotropic systems, it is useful to define VACF along a given axis,

$$C_{vv;\alpha\alpha}(t; \mathbf{n}) \doteq \frac{1}{3}\langle v_\alpha(t_0; \mathbf{n}) \cdot v_\alpha(t_0 + t; \mathbf{n})\rangle_{t0}, \tag{5}$$

where $v_\alpha(t_0; \mathbf{n})$ is given by

$$v_\alpha(t_0; \mathbf{n}) \doteq \mathbf{n} \cdot \mathbf{v}_\alpha(t). \tag{6}$$

The vector $\mathbf{n}$ is a unit vector defining a space-fixed axis.

$$\text{DOS}(n\Delta v) \doteq \sum_\alpha \omega_\alpha \tilde{C}_{vv;\alpha\alpha}(n\Delta v). \tag{7}$$

We additionally calculated the phonon spectral function, Grüneisen parameters by using the temperature-dependent effective potential (TDEP) method [25,26]. The Grüneisen parameters, which describe the volume dependence of phonon frequency of the sth phonon mode at wave vector $\mathbf{q}$, can be calculated from the third-order force constants as follows:

$$\gamma_{\mathbf{q}s} = -\frac{V}{\omega_{\mathbf{q}s}}\frac{\partial \omega_{\mathbf{q}s}}{\partial V} = -\frac{1}{6\omega_{\mathbf{q}s}^2}\sum_{ijk\alpha\beta\gamma}\frac{\epsilon_{\mathbf{q}s}^{i\alpha\dagger}\epsilon_{\mathbf{q}s}^{j\beta}}{\sqrt{m_i m_j}}r_k^\gamma \Phi_{ijk}^{\alpha\beta\gamma}e^{i\mathbf{q}\cdot\mathbf{r_j}}$$

where $\epsilon_{\mathbf{q}s}^{i\alpha}$ is the component α of the corresponding eigenvector ϵ of the ith atom, m_i is the mass of the ith atom, and $\mathbf{r}_i$ is the position vector of the ith atom. We used a $16 \times 16 \times 8$ set of $\mathbf{q}$ points in TDEP and a $4 \times 4 \times 2$ grid of $\mathbf{k}$ points in the AIMD calculations. For electron-phonon calculations, we used the plane-wave pseudopotential method in QUANTUM ESPRESSO [27–29]. We selected 884 $\mathbf{k}$ and $\mathbf{q}$ points and a 90-Ry cutoff energy for the wave function, using the optimized tetrahedron method and the PBEsol functional. The PBEsol functional can produce the most accurate phonon dispersion profile when compared directly to the measured data [30].

III. RESULTS AND DISCUSSION

Figure 2 shows the energy scans at several different Q positions with a 0.5-meV step size on Taipan at 300 K. Theoretically the phonon modes should be symmetric across both $(2 + q, 0, 0)$ and $(2 - q, 0, 0)$; however, due to instrumental resolution focusing effects, the detector presents a better profile measured on $(2 - q, 0, 0)$. We thus measured the longitudinal acoustic (LA) mode via energy scans in the Γ-X zone on $(2 - q, 0, 0)$ at 300 K and chose four points between the zone center and zone boundary, as shown in Fig. 2(b). To fit the energy scan at $(1.8, 0, 0)$ as an example, we introduce two Gaussian peaks (one for the decreasing Bragg peak tail, and the other for the phonon excitation) to fit the total scattering. The phonon excitations were expected to exhibit resolution-limited Gaussian peak profiles, each which had a full width at half maximum (FWHM) value ~ 1 meV, which is equivalent to the energy resolution of Taipan in this configuration. This was confirmed from the fit of the excitation at $(1.8, 0, 0)$ with a peak energy $\sim 3.4 \pm 0.2$ meV and a FWHM $\sim 1.4 \pm 0.5$ meV. Similar fits were performed on all data sets, as shown in Fig. 2(b). These illustrate the Q dependence of the propagation of the LA phonons along the $(q, 0, 0)$ direction. Based on the sample alignment, we measured the transverse acoustic phonon modes in $(q, 0, 3)$ directions. Further, we conducted longitudinal (LA) and transverse acoustic (TA) mode energy scans in the Γ-Z zone, with four different q values between the zone center and zone boundary, which are shown in Figs. 2(c) and 2(d). The experimental neutron intensity was fitted with Gaussian peaks, similar to the longitudinal scans. The experimental LA and TA phonon peak positions and error bars are summarized in Fig. 2(e) with star symbols.

The inelastic neutron-scattering intensities for the optical phonons at 25 K are shown in Fig. 3, with an energy transfer range from 10 to 30 meV. The data were taken at the zone centers and boundaries of Γ-X and Γ-Z zones [$Q = (200)$, (300), (003), and (003.5)]. One can see the optical phonons are populated in this region. The highest energy optical phonon of
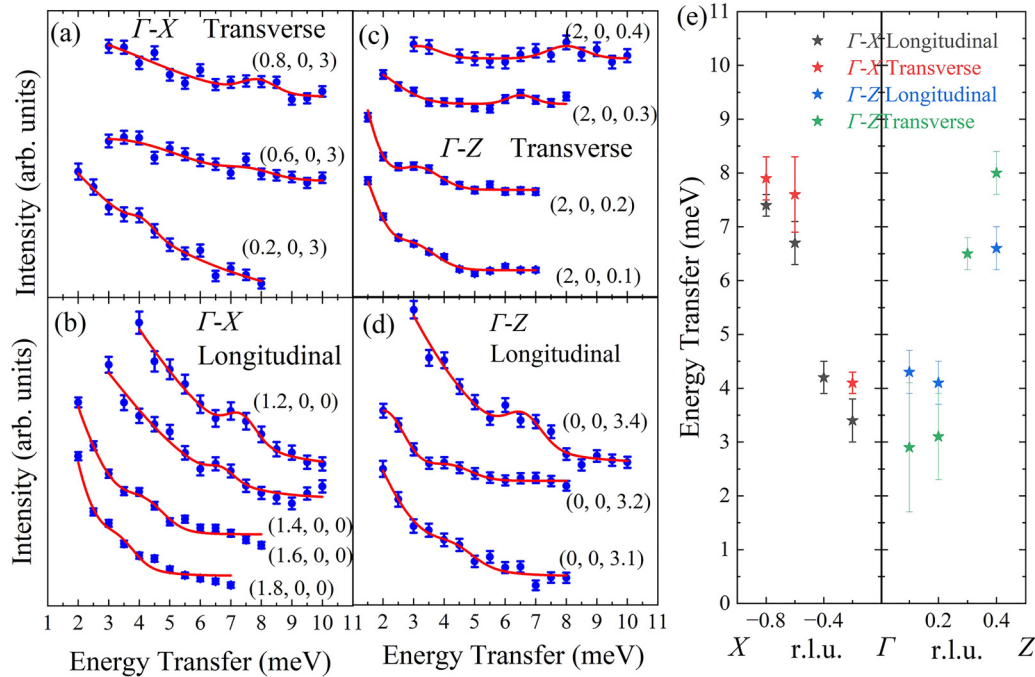
FIG. 2. The inelastic neutron-scattering results in ZrGeSe single crystals. (a)–(d) The transverse and longitudinal scans in the Γ-X zone and Γ-Z zone, respectively. The blue star symbols with error bar are experimental results, which are fitted with the red curves. The fitting results are summarized in panel (e).

ZrGeSe was observed at a slightly lower energy than the DFT calculation for the same mode ($\sim$31 meV [12]).

While each scan was collected with the same scattering statistics (per 1.3×10^9 monitor), the zone-boundary scan for the (300) shows a higher scattering intensity below 15 meV, which may be the broad tail of the scattering from the zone-boundary acoustic mode. From the DFT calculations, we expect multitple optical modes to be present within the scattering observed between 14 and 27 meV and have thus fit multiple Gaussian profiles to the clearest upper- and lower-

energy features within this band, as shown in Figs. 3(b)–3(e). The clearest features are summarized in Fig. 4. One can observe the calculated optical phonon modes of ZrGeSe, populated between 10 and 30 meV in Fig. 4, which have a low dispersion.

Further, we plot all observed phonon modes, together with the AIMD calculated phonon spectral function at 300 K. Except for the aforementioned phonons, we also obtained the LA phonons in the Γ-Z zone, and optical phonons in the Z-R zone, as shown in Fig. 4(a). Note thatthe calculated phonon bands
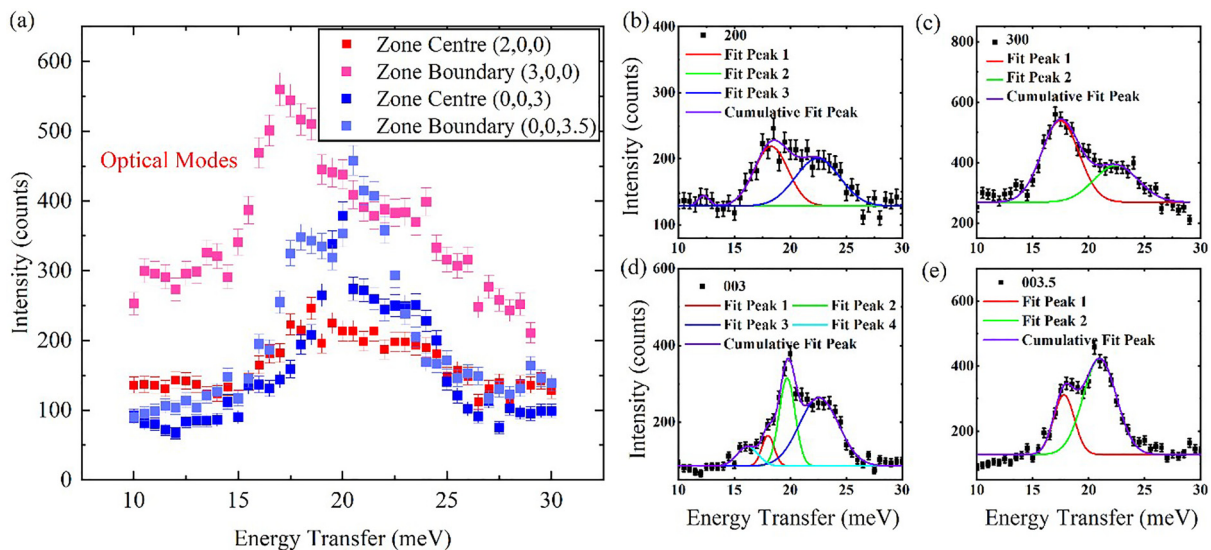

FIG. 3. (a) Optical phonons of the Γ-X and Γ-Z zones, measured both at zone center and zone boundary. (b)–(e) The fittings of the optical modes.
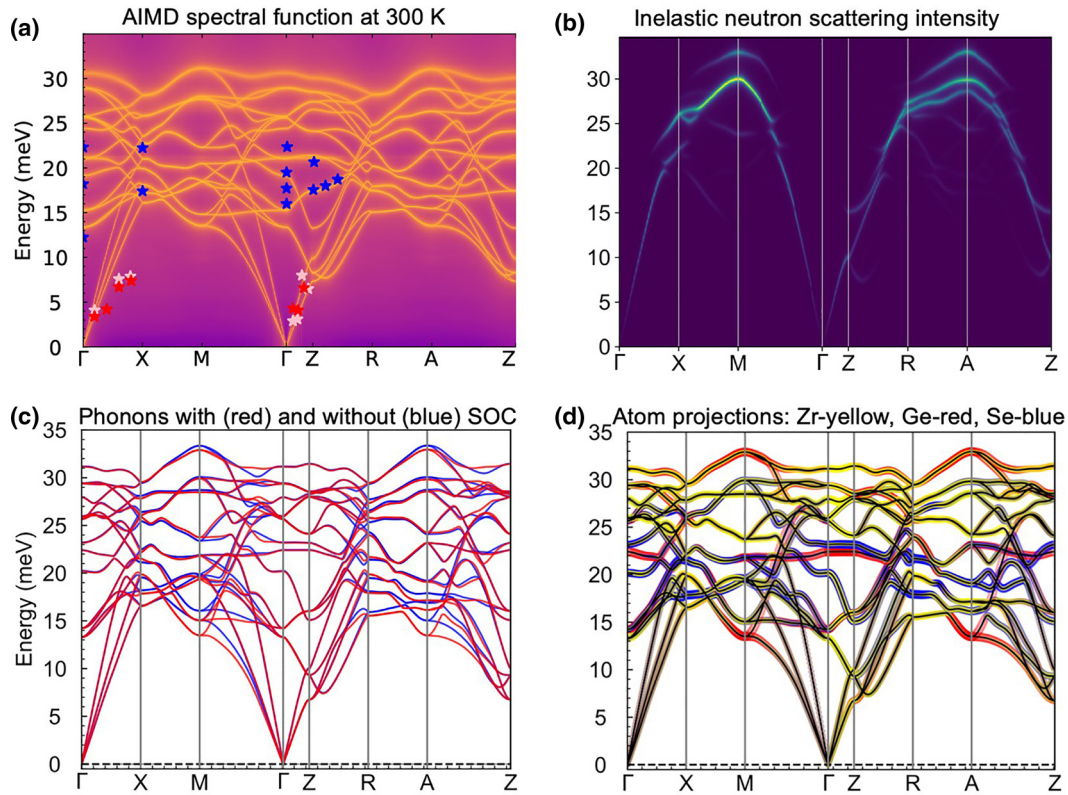
FIG. 4. Impact of different factors on the phonon dispersions of ZrGeSe. (a) Calculated AIMD phonon spectral function at 300 K and phonon dispersions of ZrGeSe, along with the observed phonons from the inelastic neutron-scattering experiments: blue star symbols are optical phonons; the pink and red symbols are transverse and longitudinal acoustic phonons. (b) Calculated inelastic neutron-scattering intensity at 300 K by using the phonon data from DFPT with SOC at equilibrium. (c) Comparisons of phonon dispersions of ZrGeSe with (red) and without (blue) the spin-orbit coupling (SOC) effect at equilibrium. (d) Atom projected phonon dispersions of ZrGeSe with SOC at equilibrium. The yellow, red, and blue points indicate the contributions of Zr, Ge, and Se atoms to the corresponding phonon band, respectively.

using the GGA-PBE functional are shown in Supplemental Material Fig. S1 [31], which is very close to the calculated phonon bands using the GGA-PBEsol functional (blue lines) in Fig. 4(c), suggesting no significant effect of including functionals. In the Γ-Z zone, the observed phonons have a similar energy range with the calculated modes. Overall, the experimental optical phonons are observed within a lower-energy band than the DFT and density functional perturbation theory (DFPT) results. Specifically, the low-energy optical phonon energy in the Z-R zone slightly increases from Z to R, which agrees with the calculated energy increase of the optical phonons from Z to R. The observed LA [red symbols in Fig. 4(a)] and TA (pink symbols) phonon modes in the Γ-X zone are consistently lower in energy compared to the calculations. To investigate it further, we calculated coherent inelastic neutron-scattering intensity [Fig. 4(b)] from DFPT data, which clearly shows that these modes (experimental phonon modes in the Γ-X zone) are not the weakest modes.

Comparing the experimental phonon peaks and lattice dynamic calculations, one may notice that the phonons are typically softer (lower in energy) in the experimental data, especially in the ab plane. Previous studies of ZrSiS by time- and angle-resolved photoemission spectroscopy suggested the electron-phonon interaction plays an important role, which is also the case in other isostructural TNLS materials [32]. We

argue that the ab−plane phonon softening can result from (i) strong spin-orbit coupling (SOC) effects, (ii) phonon-phonon interactions (anharmonic), and (iii) electron-phonon interactions. Figure 4(c) shows the calculated phonon dispersion by using DFPT with (red lines) and without SOC (blue lines), which demonstrates no noticeable SOC effect on the phonon modes in the Γ-X zone, ruling out the first reason of phonon softening. Projected atoms in the projected band structure [Fig. 4(d)] clearly shows that acoustic phonon modes in the Γ-X zone are induced from all atoms, i.e., Zr, Ge, and Se.

It is well known that anharmonic effects, which are not included in standard lattice dynamics, can lead to shifts in the phonon energy, including softening, which are strongly temperature dependent. To confirm whether anharmonic effects played a role, we employed AIMD simulations, which self-consistently include anharmonicity, to estimate the phonon DOS at the experimental temperatures (25 and 300 K). As shown in Fig. 5(a), the calculated phonon DOS at room temperature and low temperature are significantly different with regard to the highest optical phonon energy, e.g., the highest optical phonon energy at 25 K is ∼28 meV, and at 300 K is ∼32 meV. This temperature dependence of the upper phonon modes may be due to phonon softening resulting from anharmonicity in the lattice. Figure 3(a) shows the experimental optical phonons are between 12 and 27 meV at 25 K,
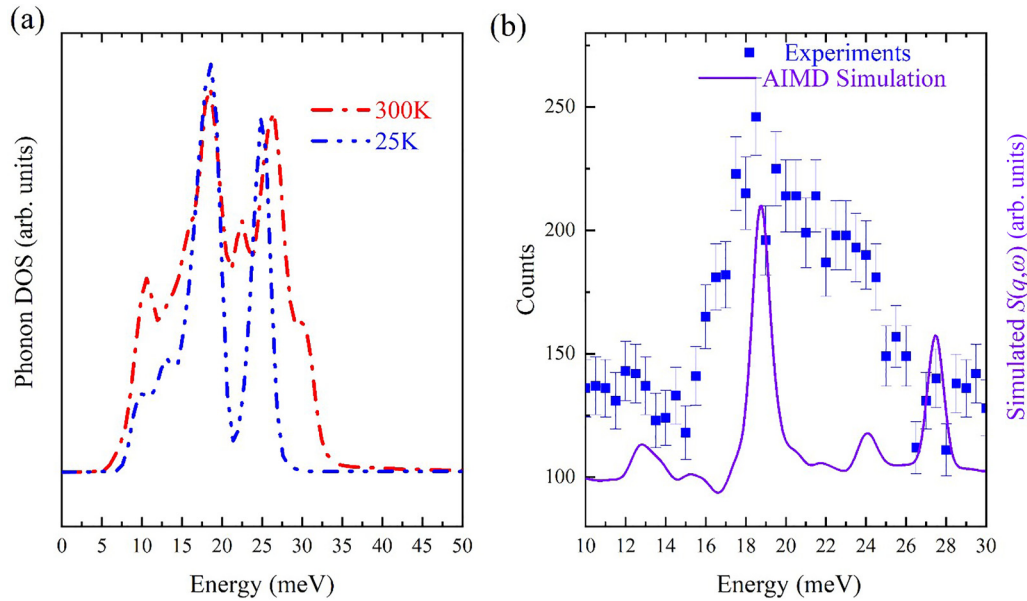
FIG. 5. (a) AIMD simulation of the total phonon DOS in ZrGeSe at 25 and 300 K. (b) Experimental observation of optical phonons at the Γ point (200), as well as the simulated phonon DOS, both at 25 K.

which agrees relatively well with the AIMD simulations. The AIMD simulated phonon DOS at 25 K and the experimental observation of optical phonons are plotted in Fig. 5(b). To investigate the origin of the phonon softening further, we calculated the mode Grüneisen parameter (Fig. 6).

The Grüneisen parameter (γ) indicates how much stress is induced when the system is heated/elongated, and hence, determines the phonon-phonon scattering (anharmonicity), i.e., the larger the values γ, the stronger the anharmonicity, and vice versa. Along the Γ-*X* direction, the γ of acoustic phonons ranges between ∼0.6 and 1.5 at 300 K, suggesting a relatively weak anharmonicity. Only the third acoustic phonon has the highest value, reaching above 2 at Γ-*Z*, suggesting relatively strong anharmonicity. The smaller values of the mode

Grüneisen parameter in ZrGeSe suggest a negligible change in the phonon frequency due to the volume change with temperature (25–300 K). The negative values of gamma in Γ-*M* suggest either a precursor of phase transitions or signatures of electron-phonon coupling [33], which will be discussed in the next section. Thus, the values of γ are not large enough (<2.5, where the average should be larger than 2.5) [34] to lead to the observed phonon softening, ruling out the second origin. We therefore consider the alternate hypothesis of strong electron-phonon interactions, initially considering the electronic band structure of this system.

The computed electron dispersions show the semimetallic nature [Fig. 7(a)], where the four bands near the Fermi level contain drumhead surface states [inset of Fig. 7(a)]. A recent experimental study suggested that surface states exist along the Γ-*X*-*M* directions, where the kink in the linear dispersion was observed along the *M*-*X* directions [35]. By investigating the correlation of the kink with electron-phonon coupling, as well as phonon softening, we calculated phonon dispersions and mode-resolved electron-phonon coupling [Fig. 7(b)] with the SOC effect.

Finally, we tested the effects of the electron-phonon interaction on the phonon modes of ZrGeSe in Fig. 7(b); the orange circles represent the mode-resolved electron-phonon coupling constant ($\lambda_{\mathbf{q}v}$), where $\lambda_{\mathbf{q}v}$ is given by

$$\lambda_{\mathbf{q}v} = \frac{2 \sum_{mn} \sum_{\mathbf{k}} \left| g_{\mathbf{k+q, k}}^{\mathbf{q}v, \, mn} \right|^2 \delta(E_{\mathbf{k+q},m} - E_F) \delta(E_{\mathbf{k},n} - E_F)}{N(E_F) \, \omega_{\mathbf{q}v}}.$$

Here $N(E_F)$, $g_{k+q, \, k}^{qv, \, mn}$, and ω_{qv}, are the electronic DOS at the Fermi level E_F, the electron-phonon coupling matrix for electron wave vector **k** and phonon wave vector **q**, and the phonon energy, respectively. The values of $\lambda_{\mathbf{q}v}$ are directly proportional to the radius of the circles, i.e., the larger the circles, the higher $\lambda_{\mathbf{q}v}$, the stronger the electron-phonon coupling, and vice versa. In ZrGeSe, significant electron-phonon
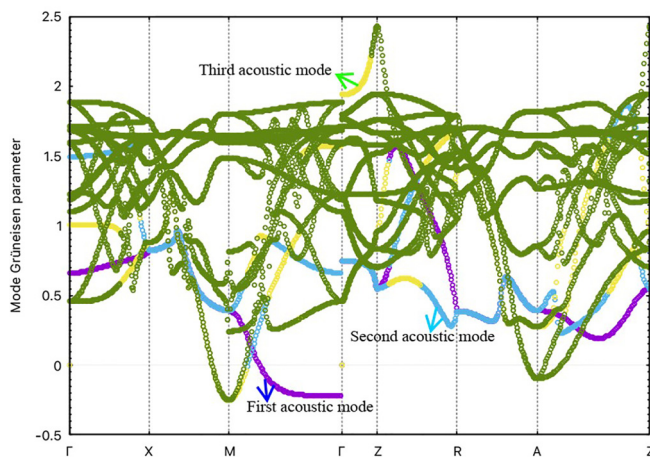

FIG. 6. Computed mode Grüneisen parameter at 300 K by using third-order force constant from AIMD. The Grüneisen parameter of optical modes are represented by colored symbols: purple symbols for the first acoustic mode, blue symbols for the second acoustic mode, and yellow symbols for the third acoustic mode.
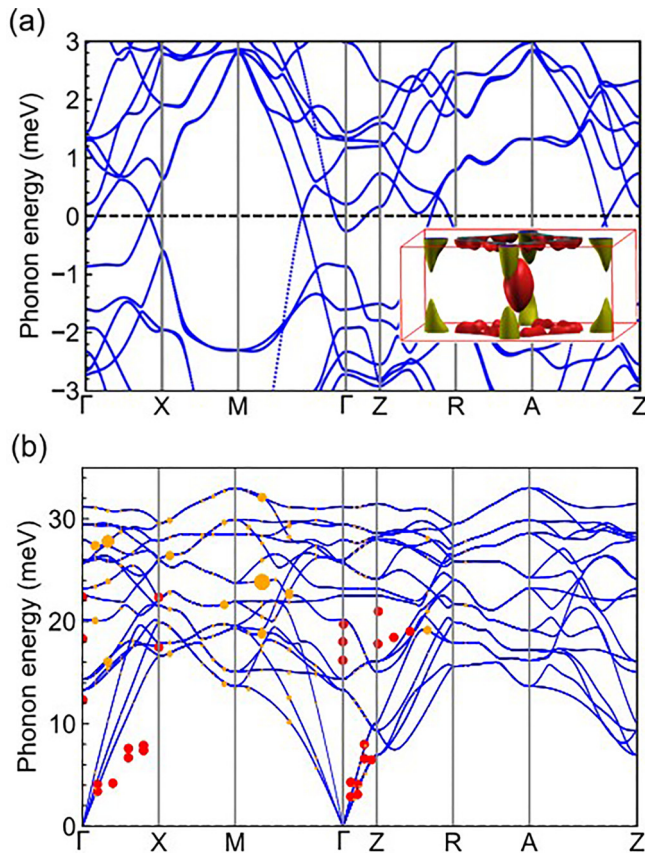
FIG. 7. (a) Electron dispersion of ZrGeSe by using the PBEsol functional. The zero energy indicates the Fermi level. The inset figure shows the Fermi surface within the first Brillouin zone. (b) Phonon dispersion of ZrGeSe by using the PBEsol functional. Red circles are the measured phonon dispersions. Orange circles are mode-resolved electron-phonon coupling constants (λ), where the radius of the circles is proportional to the strength of λ.

coupling only exists along the Γ-X direction. Notably, the electron-phonon coupling is stronger for certain modes and along the Γ-X and M-Γ directions, where experimentally the phonon softening (along Γ-X) is also observed. As the

temperature can strengthen the electron-phonon interactions, the results suggest that electron-phonon coupling can lead to phonon softening along the Γ-X direction and to an anomalous temperature dependence in the phonon band structure. This is consistent with the recent study that electron-phonon coupling can induce phonon softening in FeCoSi, where the latter study also ruled out the phonon-phonon interactions (anharmonic) as the origin of phonon softening [36].

IV. CONCLUSION

In conclusion, we have investigated phonons in the topological nodal-line semimetal ZrGeSe using inelastic neutron scattering. In the ($h0l$) scattering plane, we observed both acoustic and optical phonons at low temperature (25 K) and room temperature (300 K). The phonons were observed to be slightly softer than earlier zero-temperature DFT lattice-dynamics calculations, e.g., the experimental optical phonon range is 10–30 meV, which is smaller than the highest calculated optical phonon at ∼31 meV. The softening effect on acoustic phonons in the Γ-X zone were also observed. The softening observed in the lattice vibration modes is possibly mediated by the electron-phonon interactions [32]. In the future, it will be important to study the thermal transport behavior in ZrGeSe. Our inelastic neutron results and the simulations demonstrate the unexpected lattice dynamics in ZrGeSe single crystals due to their strong coupling with the topological electronic band structure, which could lead to strongly anisotropic thermal transport.

[1] M. G. Vergniory, L. Elcoro, C. Felser, N. Regnault, B. A. Bernevig, and Z. Wang, A complete catalogue of high-quality topological materials, Nature (London) **566**, 480 (2019).

[2] B. Yan and S.-C. Zhang, Topological materials, Rep. Prog. Phys. **75**, 096501 (2012).

[3] C. Fang, H. Weng, X. Dai, and Z. Fang, Topological nodal line semimetals, Chin. Phys. B **25**, 117106 (2016).

[4] M. Neupane et al., Observation of topological nodal fermion semimetal phase in ZrSiS, Phys. Rev. B **93**, 201104(R) (2016).

[5] L. M. Schoop et al., Dirac cone protected by non-symmorphic symmetry and three-dimensional Dirac line node in ZrSiS, Nat. Commun. **7**, 11696 (2016).

[6] R. Singha et al., Large nonsaturating magnetoresistance and signature of nondegenerate Dirac nodes in ZrSiS, Proc. Natl. Acad. Sci. USA **114**, 2468 (2017).

[7] M. N. Ali et al., Butterfly magnetoresistance, quasi-2D Dirac Fermi surface and topological phase transition in ZrSiS, Sci. Adv. **2**, e1601742 (2016).

[8] J. Hu et al., Evidence of topological nodal-line fermions in ZrSiSe and ZrSiTe, Phys. Rev. Lett. **117**, 016602 (2016).

[9] Z. Zhu et al., Quasiparticle interference and nonsymmorphic effect on a floating band surface state of ZrSiSe, Nat. Commun. **9**, 4153 (2018).

[10] T. Nakamura et al., Evidence for bulk nodal loops and universality of Dirac-node arc surface states in ZrGeX_c(X_c = S, Se, Te), Phys. Rev. B **99**, 245105 (2019).

[11] L. Guo et al., Electronic transport evidence for topological nodal-line semimetals of ZrGeSe single crystals, ACS Appl. Electron. Mater. **1**, 869 (2019).

[12] B. Salmankurt and S. Duman, First-principles study of structural, mechanical, lattice dynamical and thermal properties of nodal-line semimetals ZrXY (X = Si, Ge; Y = S, Se), Philos. Mag. **97**, 175 (2017).

[13] T. Zhang, Z. Song, A. Alexandradinata, H. Weng, C. Fang, L. Lu, and Z. Fang, Double-Weyl phonons in transition-metal monosilicides, Phys. Rev. Lett. **120**, 016401 (2018).

[14] B. W. Xia, R. Wang, Z. J. Chen, Y. J. Zhao, and H. Xu, Symmetry-protected ideal type-II Weyl phonons in CdTe, Phys. Rev. Lett. **123**, 065501 (2019).

[15] R. Wang, B. W. Xia, Z. J. Chen, B. B. Zheng, Y. J. Zhao, and H. Xu, Symmetry-protected topological triangular Weyl complex, Phys. Rev. Lett. **124**, 105303 (2020).

[16] J. Li *et al.*, Computation and data driven discovery of topological phononic materials, Nat. Commun. **12**, 1204 (2021).

[17] L. Zhang, J. Ren, J. S. Wang, and B. Li, Topological nature of the phonon Hall effect, Phys. Rev. Lett. **105**, 225901 (2010).

[18] S. Singh, Q. S. Wu, C. Yue, A. H. Romero, and A. A. Soluyanov, Topological phonons and thermoelectricity in triple-point metals, Phys. Rev. Mater. **2**, 114204 (2018).

[19] K. C. Rule, R. A. Mole, and D. Yu, Which glue to choose? A neutron scattering study of various adhesive materials and their effect on background scattering, J. Appl. Crystallogr. **51**, 1766 (2018).

[20] A. Togo and I. Tanaka, First principles phonon calculations in materials science, Scr. Mater. **108**, 1 (2015).

[21] J. P. Perdew, K. Burke, and M. Ernzerhof, Generalized gradient approximation made simple, Phys. Rev. Lett. **77**, 3865 (1996).

[22] S. Grimme, Semiempirical GGA-type density functional constructed with a long-range dispersion correction, J. Comput. Chem. **27**, 1787 (2006).

[23] W. Humphrey, A. Dalke, and K. Schulten, VMD: Visual molecular dynamics, J. Mol. Graphics **14**, 33 (1996).

[24] T. Róg *et al.*, *n*Moldyn : A program package for a neutron scattering oriented analysis of molecular dynamics simulations, J. Comput. Chem. **24**, 657 (2003).

[25] O. Hellman, I. A. Abrikosov, and S. I. Simak, Lattice dynamics of anharmonic solids from first principles, Phys. Rev. B **84**, 180301(R) (2011).

[26] O. Hellman and I. A. Abrikosov, Temperature-dependent effective third-order interatomic force constants from first principles, Phys. Rev. B **88**, 144301 (2013).

[27] P. Giannozzi *et al.*, Advanced capabilities for materials modelling with QUANTUM ESPRESSO, J. Phys.: Condens. Matter **29**, 465901 (2017).

[28] P. Giannozzi *et al.*, QUANTUM ESPRESSO: A modular and open-source software project for quantum simulations of materials, J. Phys.: Condens. Matter **21**, 395502 (2009).

[29] P. Giannozzi *et al.*, QUANTUM ESPRESSO toward the exascale, J. Chem. Phys. **152**, 154105 (2020).

[30] L. He, F. Liu, G. Hautier, M. J. T. Oliveira, M. A. L. Marques, F. D. Vila, J. J. Rehr, G. M. Rignanese, and A. Zhou, Accuracy of generalized gradient approximation functionals for density-functional perturbation theory calculations, Phys. Rev. B **89**, 064305 (2014).

[31] See Supplemental Material at http://link.aps.org/supplemental/10.1103/PhysRevMaterials.8.034201 for more experimental and simulation results.

[32] Y. Liu *et al.*, Ultrafast relaxation of acoustic and optical phonons in a topological nodal-line semimetal ZrSiS, Commun. Phys. **5**, 203 (2022).

[33] M. Krisch *et al.*, Phonons of the anomalous element cerium, Proc. Natl. Acad. Sci. USA **108**, 9342 (2011).

[34] W. Qiu *et al.*, Part-crystalline part-liquid state and rattling-like thermal damping in materials with chemical-bond hierarchy, Proc. Natl. Acad. Sci. USA **111**, 15031 (2014).

[35] Z. Cheng *et al.*, Visualizing Dirac nodal-line band structure of topological semimetal ZrGeSe by ARPES, APL Mater. **7**, 051105 (2019).

[36] A.-M. Racu, D. Menzel, J. Schoenes, and K. Doll, Crystallographic disorder and electron-phonon coupling in $Fe_{1-x}Co_xSi$ single crystals: Raman spectroscopy study, Phys. Rev. B **76**, 115103 (2007).